Valproic acid-induced changes of 4D nuclear morphology in astrocyte cells

Alexandr A. Kalinin[a,b,c], Xinhai Hou[a,b,d], Alex S. Ade[b], Gordon-Victor Fon[b], Walter Meixner[b], Gerald A. Higgins[b], Jonathan Z. Sexton[e,f,g], Xiang Wan[a], Ivo D. Dinov[b,c,h], Matthew J. O'Meara[b], and Brian D. Athey[b,h,i,*]

[a]Shenzhen Research Institute of Big Data and [d]School of Science and Engineering, Chinese University of Hong Kong–Shenzhen, Shenzhen 518172, Guangdong, China; [b]Department of Computational Medicine and Bioinformatics, [c]Statistics Online Computational Resource (SOCR), Health Behavior and Biological Sciences, [e]Department of Internal Medicine, Gastroenterology, Michigan Medicine, [f]Department of Medicinal Chemistry, College of Pharmacy, [g]Center for Drug Repurposing; [h]Michigan Institute for Data Science (MIDAS), and [i]Department of Psychiatry, University of Michigan, Ann Arbor, MI 48109

ABSTRACT **Histone deacetylase inhibitors, such as valproic acid (VPA), have important clinical therapeutic and cellular reprogramming applications. They induce chromatin reorganization that is associated with altered cellular morphology. However, there is a lack of comprehensive characterization of VPA-induced changes of nuclear size and shape. Here, we quantify 3D nuclear morphology of primary human astrocyte cells treated with VPA over time (hence, 4D). We compared volumetric and surface-based representations and identified seven features that jointly discriminate between normal and treated cells with 85% accuracy on day 7. From day 3, treated nuclei were more elongated and flattened and then continued to morphologically diverge from controls over time, becoming larger and more irregular. On day 7, most of the size and shape descriptors demonstrated significant differences between treated and untreated cells, including a 24% increase in volume and 6% reduction in extent (shape regularity) for treated nuclei. Overall, we show that 4D morphometry can capture how chromatin reorganization modulates the size and shape of the nucleus over time. These nuclear structural alterations may serve as a biomarker for histone (de-)acetylation events and provide insights into mechanisms of astrocytes-to-neurons reprogramming.**

Monitoring Editor
Jennifer Lippincott-Schwartz
Howard Hughes Medical Institute

Received: Aug 24, 2020
Revised: Mar 16, 2021
Accepted: Apr 23, 2021

INTRODUCTION

Multicellular organisms regulate their cell type and state by selectively exposing portions of their genome for transcription through the spatial and temporal organization of chromatin—dubbed the 4D nucleome (Chen *et al.*, 2015; Cremer *et al.*, 2015; Higgins *et al.*, 2015, 2017a). Structurally, 3D conformation of the genome involves 1.65 turns of DNA wrapped onto a histone octamer, creating nucleosomes linked as beads-on-a-string, which are then wrapped into chromatin fibers and higher-order loops, organizing into topologically associating domains (TADs). Finally, TADs collect into a diploid set of chromosome territories (Higgins *et al.*, 2015, 2017a). Histones accommodate a range of posttranslational modifications, which are controlled by epigenetic proteins that ultimately regulate the transcriptional state of the cell and mediate mechanical protection of genome by chromatin rigidity (Yang and Seto, 2007; Stephens *et al.*, 2019). Chemicals that target these proteins can be used to modulate chromatin states and the concomitant cell and nuclear morphology changes observed in human diseases (Marchion *et al.*, 2005; Stephens *et al.*, 2019). For example, valproic acid (VPA) is a histone deacetylase inhibitor used clinically to treat epilepsy, bipolar disorders, social phobias, and neuropathic pain (Göttlicher *et al.*, 2001; Ganai *et al.*, 2015). Mechanistically, VPA shifts the balance toward greater histone acetylation, DNA exposure, and chromatin decondensation; activating transcriptional programs that regulate cellular

This article was published online ahead of print in MBoC in Press (http://www.molbiolcell.org/cgi/doi/10.1091/mbc.E20-08-0502) on April 28, 2021.

*Address correspondence to: Brian D. Athey (bleu@umich.edu).

Abbreviations used: AUC, area under the receiving operator characteristic curve; NHAs, normal human astrocytes; SVM, support vector machine; TADs, topologically associating domains; VPA, valproic acid.

processes related to cancer (Göttlicher *et al.*, 2001; Eckschlager *et al.*, 2017), traumatic brain injury (Higgins *et al.*, 2017b), ischemia (Pickell *et al.*, 2020), as well as cellular reprogramming (Huangfu *et al.*, 2008). An outstanding question, however, is to characterize how mesoscale nuclear structures such as TADs mediate the effects of VPA and other epigenetic modulators on cellular morphology. However, limitations of the emerging technologies that can capture these nanoscale (histone marks) and mesoscale (nuclear architecture) phenomena, including optical microscopy, ATACseq, and single cell RNAseq, make it difficult to simultaneously monitor macroscale (cellular morphology) cellular state.

Recent mechanobiology studies revealed the role of chromatin as a key regulator of nuclear shape (Uhler and Shivashankar, 2018; Stephens *et al.*, 2019). VPA induces increased euchromatin, which results in weakened nuclear rigidity and morphology changes that occur independently of lamins (Stephens *et al.*, 2017, 2018). Here we aim to leverage this effect for assessing how the epigenetic and mesoscale nuclear state can be characterized by the overall nuclear size and shape to probe VPA's mechanism of action. Importantly, we show that nuclear morphology can be captured in standard microscopy experiments to relate epigenetic regulators with phenotypic measurements of a cell and its organelles.

Toward this goal, we present a detailed characterization of the size and shape of astrocyte nuclei in the context of VPA treatment. We chose astrocytes because they developmentally originate from the same precursor cells as neurons and proliferate in response to brain damage (Amamoto and Arlotta, 2014), but also can be directly reprogrammed into functional neurons by sets of small molecules—often including VPA—in the lab (Cheng *et al.*, 2015; Zhang *et al.*, 2015; Gao *et al.*, 2017; Qin *et al.*, 2017). These studies, however, are not always congruent. Some reports demonstrated that VPA inhibits (Yin *et al.*, 2019) or increases reprogramming efficiency (Cheng *et al.*, 2015; Zhang *et al.*, 2015), while others suggest that VPA alone induces astrocyte reprogramming into neurons (Cheng *et al.*, 2015). The treatment protocols, concentrations, and combinations of small molecules differ between these studies, indicating that underlying mechanisms driving the transdifferentiation process are not well understood.

Existing studies that have focused on astrocyte-to-neuron reprogramming observed changes only in cellular morphology, presented in a qualitative manner. Others quantified VPA-induced nuclear morphological changes in non-astrocyte cells, reporting time-, dose-, and cell type–dependent responses. Their results ranged from no observed changes in nuclear geometry (Ganai *et al.*, 2015); to altered nuclear shape ("blebbing"), but not size (Stephens *et al.*, 2017, 2018); to increased nuclear size, either after 1 h (Felisbino *et al.*, 2011, 2014, 2016) or not earlier than after 7–14 d (Kortenhorst *et al.*, 2009) of VPA treatment. Moreover, these approaches were limited to basic 2D surrogates of geometric measures, often reporting few features such as cross-sectional nuclear area or maximum diameter. Given that chromatin is highly organized in 3D, the effects of chromatin remodeling on nuclear morphology can only be fully described in three dimensions. Supporting this assumption, there is growing practical evidence that 3D representations allow for more accurate characterizations of cell and nuclear morphology, compared with 2D measures (Choi and Choi, 2007; Meyer *et al.*, 2009; Depeursinge *et al.*, 2014; Kalinin *et al.*, 2018a; Medyukhina *et al.*, 2020). Because single-perspective 2D images depend on an object's orientation and the focal plane, they provide only a sample of its real geometry. For example, cell nuclei that differ in volume and shape can appear similarly small and circular in optically sectioned images, thus leading to lower discriminative performance of a classifier (Choi and Choi, 2007). In addition, a more comprehensive morphological representation of nuclei in 3D is more informative than resolution as a determining factor for classification performance (Meyer *et al.*, 2009). Our previous results also indicated that 3D size and shape descriptors outperform their 2D counterparts in the task of nuclear morphological classification (Kalinin *et al.*, 2018a).

Even when the 3D object is perfectly aligned with the focal plane, only the first two out of three principal axes (major, median, minor) can be measured from its 2D representation. This reduces the accuracy of shape measures computed from size features. For example, sphericity assesses the compactness of the object, that is, it measures how closely the global object shape resembles that of a perfect sphere, which is computed via volume and surface area or approximated using principal axes (Xu *et al.*, 2009). The extent (ratio of the object volume to the bounding box volume) and solidity (ratio of the object volume to the convex hull volume) of nuclear surfaces are useful measures of the amount and size of concavities (or protrusions) in an object boundary. Other shape descriptors rely on the notion of the curvature that describes how bent the curve is around each point of a surface. They allow for measuring local shape alterations that are observed on the nuclear surface and would not be exhibited in 2D projection. Mean curvature is an extrinsic measure of 3D shape that provides a balanced measure between shape morphology and curvature magnitude (Tsagkrasoulis *et al.*, 2017; Kalinin *et al.*, 2018b). Gaussian curvature is an intrinsic (scale-invariant) measure of curvature that depends only on distances that are measured on the surface. Shape index and curvedness are morphometric descriptors that can capture local shape features, independently or in relation to the size of an object (Koenderink and Van Doorn, 1992). Fractal dimension is the measure of the object's boundary complexity (Metze *et al.*, 2019). Together, these features allow one to measure various aspects of shape and provide a detailed quantitative characterization of 3D object morphology.

To address the limitations of previous studies, we quantified VPA-induced changes in the 4D nuclear morphology of primary human astrocyte cells. Our findings show that geometric descriptors extracted from voxel and surface-modeled representations of 3D nuclear shapes enabled accurate and interpretable characterization of time-dependent morphological changes in VPA-treated astrocytes. This allowed us to distinguish between nuclear morphological profiles of treated and normal astrocytes over time with a time-average accuracy of 82%. We showed that VPA treatment induced a time-dependent increase in nuclear size and nuclear shape irregularity in astrocytes over the course of treatment.

RESULTS AND DISCUSSION

Experiment and data

To determine how VPA-induced alterations of chromatin structure are reflected in 4D nuclear morphology, we treated human astrocyte cells with 1.5 mM of VPA at multiple time points (days 1, 3, and 5) and obtained volumetric images of DAPI-labeled nuclei using confocal microscopy at three time points (days 3, 5, and 7). This provided us with 4D images (3D + time) in the following conditions: normal human astrocytes (NHAs) and cells treated with VPA (Figure 1A). First, we used deconvolution to correct for background noise and spherical aberrations in original image volumes (Supplemental Figure 1). Then, we segmented individual nuclei into 3D binary voxel masks (Figure 1B). The number of nuclei identified after segmentation and quality control are listed in Table 1 for each day and treatment condition. Higher numbers of untreated nuclei compared with the treated group might be due to significant inhibition of astrocyte cell growth by VPA at concentrations over 1 mM

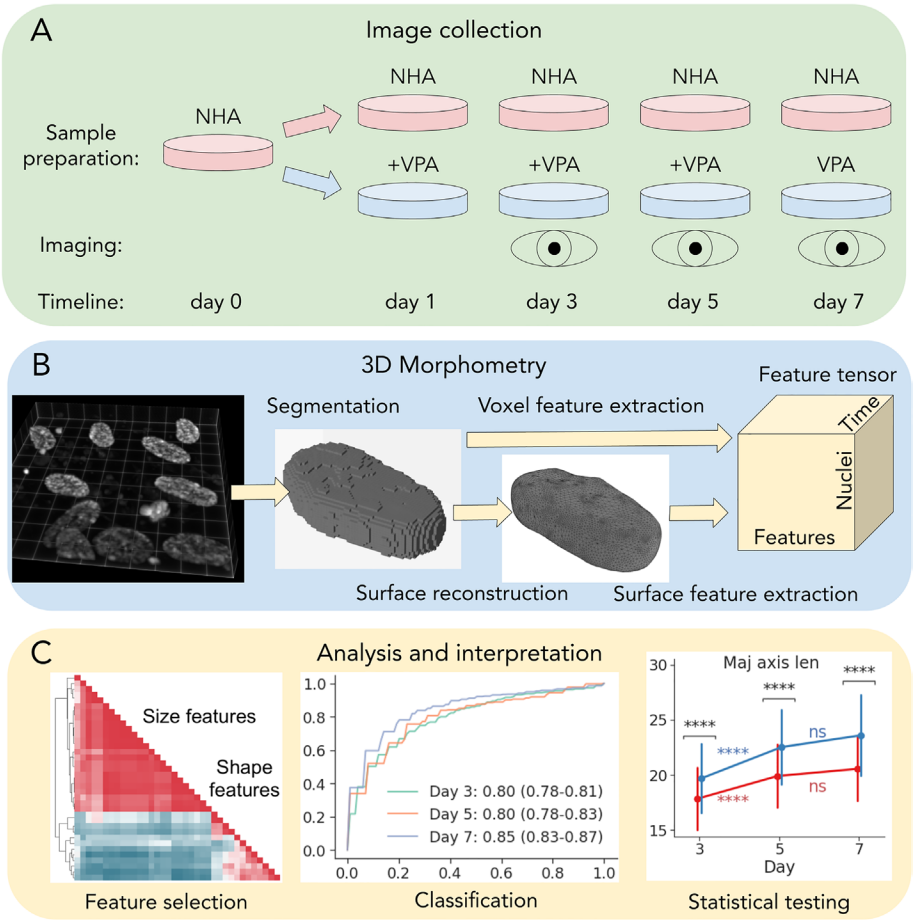

FIGURE 1: A schematic overview of the experiment, data collection, and analysis. (A) Sample preparation, treatment, and imaging. (B) 3D nuclear segmentation, shape modeling, and feature extraction. (C) Feature selection, and univariate statistical and machine learning analysis.

(Sasai *et al.*, 2007). Details of the deconvolution, segmentation, and quality control protocols can be found in the *Materials and Methods* section.

A simple approach to 3D morphometry is to extract features from binary object masks represented as voxel volumes (Dufour *et al.*, 2015). From each voxel binary mask (Figure 1B), we computed the total of 11 geometric features: volume, bounding box and convex hull volumes, extent, solidity, lengths of main axes, and inertia tensor principal components. However, voxel-based representations can be noisy and may lose fine local geometric detail or even misrepresent the object's global topological structure. We have previously shown that nuclear surfaces obtained via shape modeling are more informative and reliable for nuclear morphometry when compared with alternatives (Kalinin *et al.*, 2018b). Here, we extended that approach by extracting 16 different size and shape descriptors that can characterize morphological changes in more detail, compared with just 6 in our previous study (Kalinin *et al.*, 2018b). We obtained nuclear surface representations from 3D binary masks (Figure 1B) and measured the same descriptors as extracted from voxels, with the addition of bounding cylinder and sphere volumes, sphericity, fractal dimension, mean and Gaussian curvatures, curvedness, and shape index. The combined feature tensor containing nuclear morphological profiles (Figure 1B) was used for model and feature selection, statistical and machine learning–based analysis, and interpretation (Figure 1C).

Surface modeling provided compact and accurate characterization of 3D nuclear morphology

To evaluate the utility of different representations of nuclear morphology, we asked how well they facilitate morphological classification of NHA versus VPA cells, using time point–averaged area under the receiving operator characteristic curve (AUC) as the performance metric. Because the performance of classification algorithms varies across bioinformatics problems and datasets (Olson *et al.*, 2018) and not all models have a feature weighting mechanism, we compared the performance across eight standard classifiers that enable feature importance estimation (Supplemental Figure S2). At each timepoint, we used random subsampling of the prevalent class due to high class imbalance (Table 1). First, because voxel and surface features have not been directly compared before in terms of nuclear morphological classification, we trained each model on sets of voxel-based (*V*) and surface-based features (*S*). As a baseline, we defined 2D voxel features extracted from 3D binary mask maximum intensity projections (V_{2D}). To facilitate a fairer comparison between *V* and *S*, we also evaluated the subsets V_{sub} and S_{sub} that consisted of the 10 features that are captured by both representations (Supplemental Figure S2). As expected, the 2D feature set performed the worst (73% AUC), confirming that 3D measures provide more discriminative power. The performance was higher on the subset of voxel features (77% vs. 74% AUC on V_{sub} vs. S_{sub}), but not with full sets (77% AUC on *V* and on *S*). The best overall performance was achieved when using the combination of both voxel and surface-based features (78% AUC on *V* + *S*). Among tested classifiers, the support vector machine (SVM) model (Cortes and Vapnik, 1995) outperformed other classifiers averaged across all feature sets (81% AUC), so we chose to use this model going forward.

Clustering of the complete *V* + *S* feature set revealed two major groups, roughly corresponding to size and shape descriptors (Figure 2A). To reduce redundancy and aid interpretability, we selected seven features (S_7) from smaller subclusters that maximized SVM classification performance (82% AUC). These features included surface-based median axis length, convex hull volume, bounding

	Day		
Treatment	3	5	7
NHA	186 (–23)	163 (–18)	101 (–10)
VPA	128 (–18)	67 (–6)	78 (–15)
Total	314 (–41)	230 (–24)	179 (–35)

TABLE 1: Number of segmented astrocyte nuclear 3D binary masks per day for each treatment condition after QC (number of nuclei filtered by quality control is in parentheses).

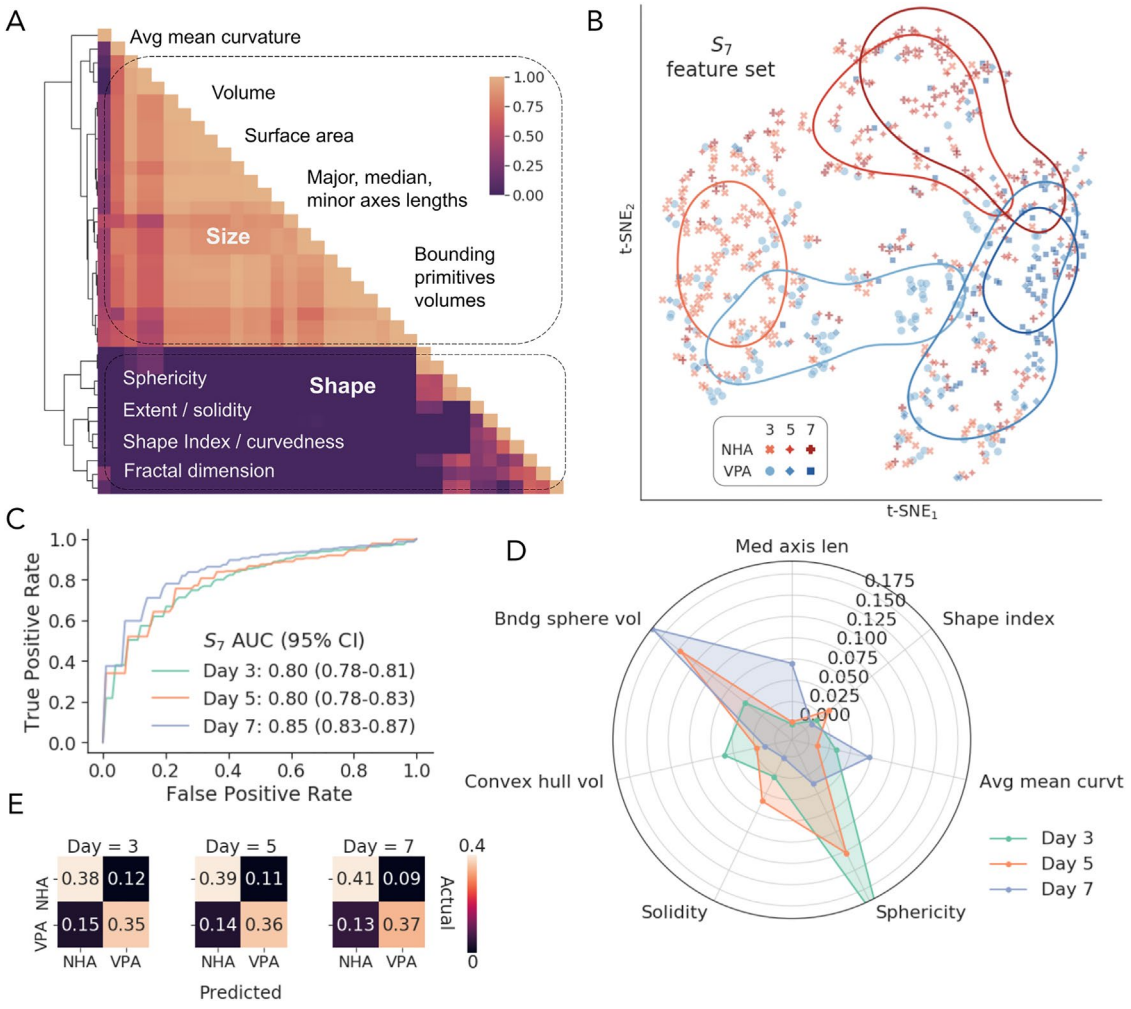

FIGURE 2: Morphological classification performance. (A) hierarchical clustering of the Pearson correlations among all voxel and surface features ($V + S$), showing representative size and shape descriptors. (B) 2D t-distributed stochastic neighbor embedding (t-SNE) of the selected feature space, showing corresponding conditions (NHA or VPA) at every time point (day 3, 5, or 7). The lines denote clusters identified by kernel density estimation. (C) Receiver operating characteristic (ROC) curves for the SVM classifier with S_7 features on days 3, 5, and 7. (D) Average normalized confusion matrices for the SVM classifier on the S_7 features. (E) SVM-estimated permutation importance of S_7 features for distinguishing nuclear morphologies on each day.

sphere volume, sphericity, average mean curvature, shape index, and voxel-based solidity. S_7 provided distinctive representations of nuclear morphological profiles at different time points, as shown by the t-distributed stochastic neighbor embedding (t-SNE; van der Maaten and Hinton, 2008) 2D projection in Figure 2B. The SVM classifier demonstrated robust performance with AUCs of 80%, 80%, and 85% on days 3, 5, and 7, respectively (Figure 2C), with classification errors that were only slightly shifted toward false negatives at each day, indicating the effectiveness of the prevalent class subsampling (Figure 2D). Relative feature ranking from the trained SVM model (Figure 2E) revealed that sphericity was the most important feature for day 3, followed by convex hull and bounding sphere volumes. On day 5, bounding sphere volume, sphericity, and solidity were the top-3 important descriptors. Bounding sphere volume was again the most important measure on day 7, followed by average mean curvature, median axis length, and sphericity. Our findings showed that both size and shape features were important for discrimination of treated and untreated nuclei, demonstrating that a combination of 3D descriptors aids in accurate morphological classification.

VPA induced increased nuclear size

We observed time-dependent alterations in astrocyte nuclear sizes as demonstrated by examples of NHA and VPA-treated reconstructed nuclear surfaces shown in Figure 3A, with the latter having increasingly longer major axis length and higher volume. To provide a more detailed characterization of changes in 3D nuclear size, we chose six size descriptors for further study; three of which were selected as a part of S_7 (median axis length, convex hull, and bounding sphere volumes), while major and minor axes lengths and nuclear volume were chosen manually for interpretability (Figure 3B). Measuring the three principal axes also allowed for the generation of inferences about the global shape of nuclei, as described in the next section. We reported each relative difference as the percentage change from the mean of the control group (NHA), along with a p value obtained using a two-sided Mann-Whitney U test with Holm–Šidák multiple testing correction, and AUC that in the case of the Mann-Whitney U test is equivalent to the common language effect size statistic (Mason and Graham, 2002).

By day 3, the average major axis length of VPA-treated nuclei compared with controls had increased by 10% ($p < 0.0001$, 70%

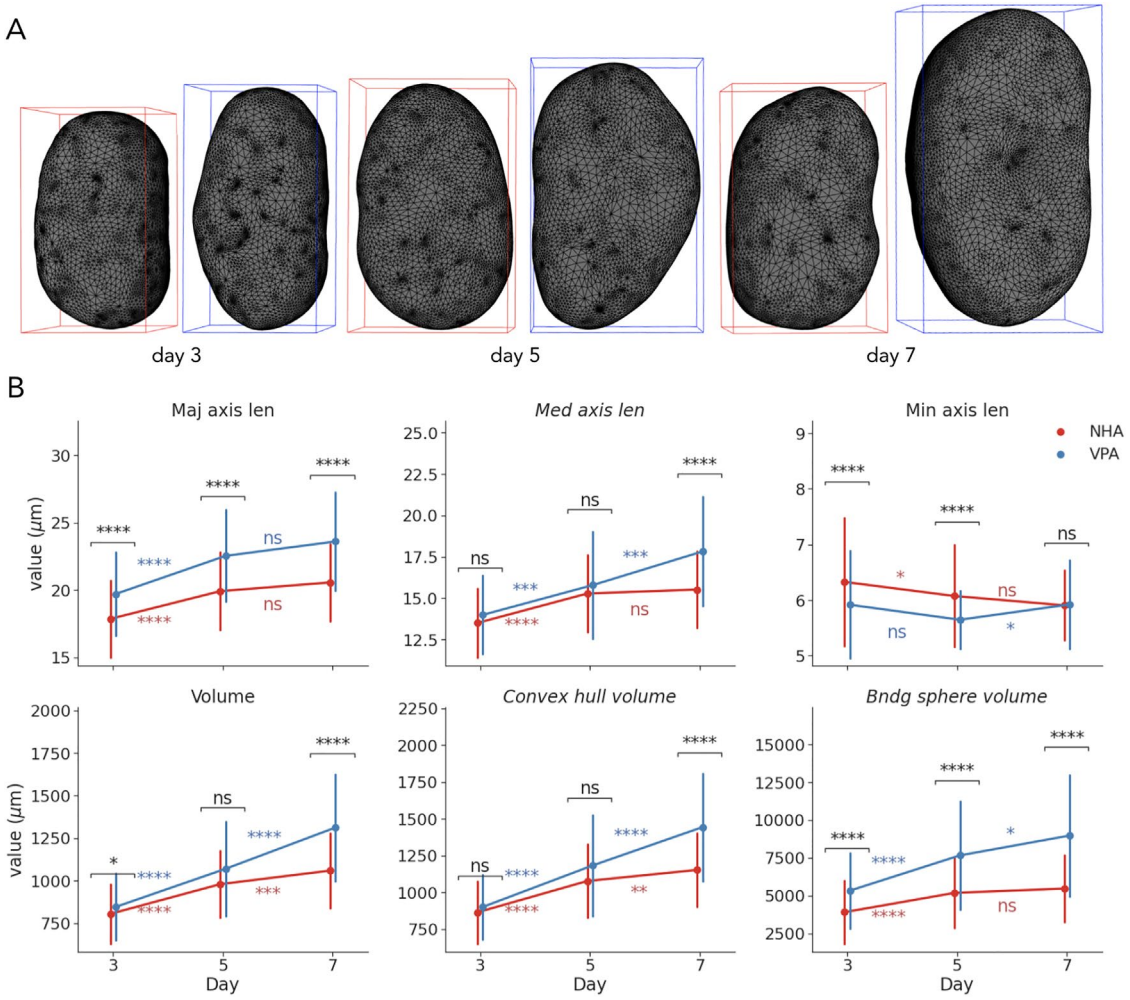

FIGURE 3: Visualization and univariate statistical analysis of size changes under VPA treatment. (A) Reconstructed surfaces of representative NHA and VPA nuclei on days 3, 5, and 7. (B) Time-dependent changes in morphometric measures of nuclear sizes (points show mean; error bars show SD; *, $p < 0.05$; **, $p < 0.01$; ***, $p < 0.001$; ****, $p < 0.0001$).

AUC), the average minor axes length had decreased by 7% ($p <$ 0.0001, 67% AUC), while there was no significant difference in median axis lengths (Figure 3B). Despite more subtle changes in nuclear (+5%, $p < 0.05$, 58% AUC) and convex (+4%, $p > 0.05$, 57% AUC) hull volumes, the volume of the bounding sphere was 36% larger ($p < 0.0001$, 74% AUC) in the VPA group. Between days 3 and 5, measures of major and median axes lengths indicated intragroup changes for both NHA (+12%, $p < 0.0001$ for major; +13%, $p <$ 0.0001 for median) and VPA nuclei (+14%, $p < 0.0001$ for major; +13%, $p < 0.001$ for median), along with a slight shortening of minor axes. Nuclear, convex hull, and bounding sphere volumes also increased in both groups, correspondingly. As a result, the treated nuclei differed from controls on day 5 by having a 13% longer major axis ($p < 0.0001$, 73% AUC) and a 4% shorter minor axis ($p < 0.0001$, 67% AUC), along with 48% larger bounding sphere volumes ($p <$ 0.0001, 74% AUC).

Between days 5 and 7, there were no significant changes in axes lengths in the control group, while the median axis length in the treated group increased by 13% ($p < 0.001$) and the minor increased by 5% ($p < 0.05$; Figure 3B). By day 7, VPA-treated nuclei had 15% larger major axes ($p < 0.0001$, 75% AUC) and 15% larger median axes ($p < 0.0001$, 70% AUC), while the minor axis length was comparable to that of the untreated nuclei. Nuclear volume and convex hull volume increased in both groups from day 5 to 7, but the change in the VPA-treated nuclei was more dramatic (+23%, $p <$ 0.0001 for volume; +22%, $p < 0.0001$ for convex hull) than in the NHA group (+8%, $p < 0.001$ for volume; +7%, $p < 0.01$ for convex hull). As a result, the treated nuclei had 24% larger volume ($p <$ 0.0001, 77% AUC), 25% larger convex hull ($p < 0.0001$, 76%), and 64% larger bounding sphere volume ($p < 0.0001$, 80% AUC), when compared with controls on day 7.

Our findings highlight a transition point between two phases of morphological changes. Before day 5, nuclear sizes in both the VPA and the NHA groups significantly increased in all reported measures, except for the minor axis length. VPA-treated nuclei demonstrated more prominent elongation and flattening, along with the slightly more rapid increase of the volume, compared with controls. NHA nuclear volumes increased less between days 5 and 7, while measures of VPA-treated nuclear size continued to increase, mostly due to longer median axes, demonstrating biggest differences by the last day, as illustrated by visualizations in Figure 3A. Finally, all individual feature AUCs were lower than those of the SVM model at each time point (Figure 2C), which highlighted the ability of a combination of 3D linear and volumetric features to

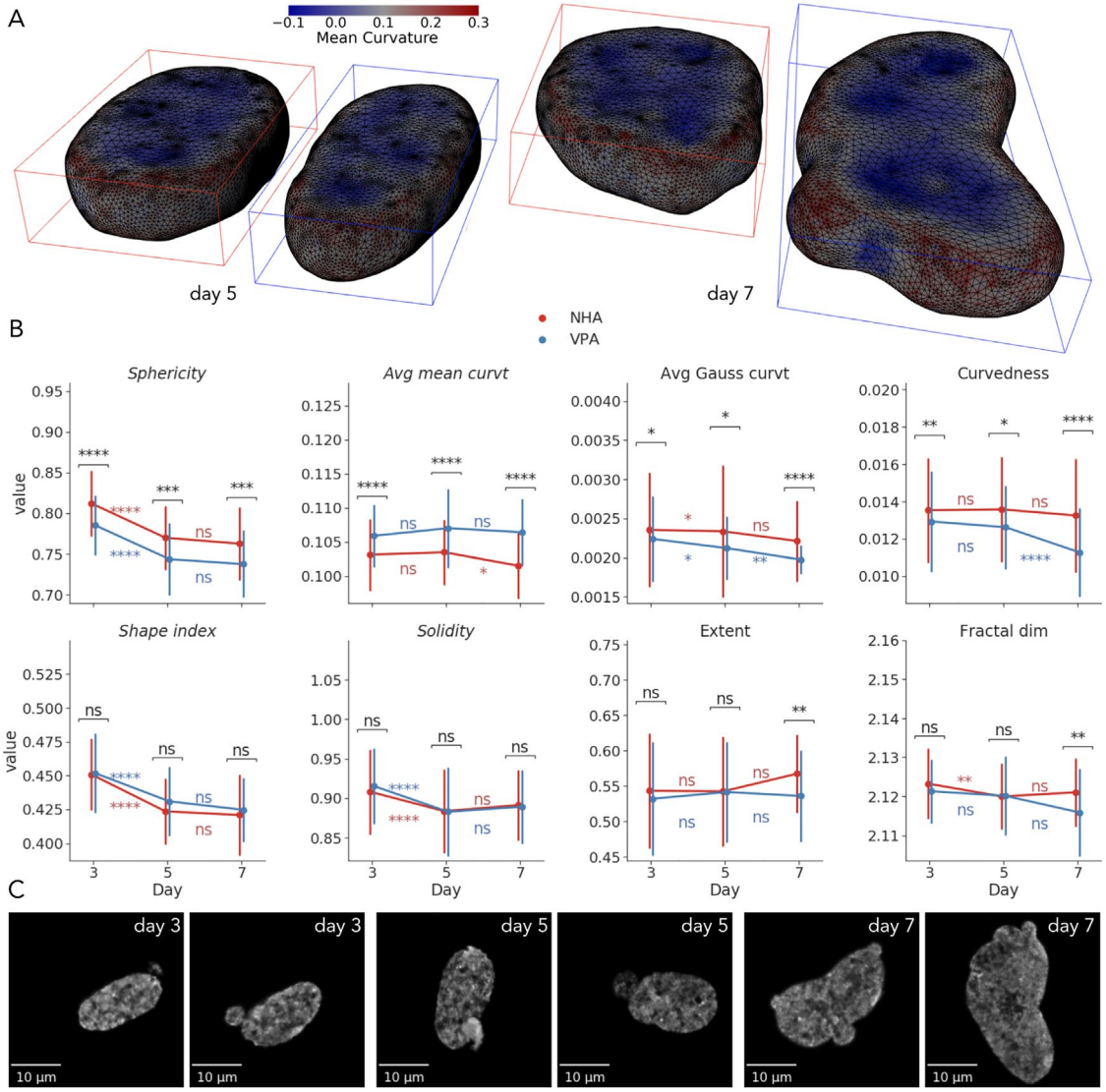

FIGURE 4: Visualization and univariate statistical analysis of shape changes under VPA treatment. (A) Reconstructed surfaces of a representative NHA and VPA nuclei on days 5 and 7, annotated with per-vertex mean curvature. (B) Time-dependent changes in morphometric measures of nuclear shapes (points show mean; error bars show SD; *, $p < 0.05$; **, $p < 0.01$; ***, $p < 0.001$; ****, $p < 0.0001$). (C) *XY* maximum intensity projections of VPA-treated nuclei with irregular shapes and blebbing.

capture size alterations that are difficult to ascertain when using solely individual measures.

VPA induced nuclear shape irregularity

Consistent with VPA decondensing the chromatin to reduce nuclear rigidity (Stephens *et al.*, 2018), we observed more globally irregular surface shapes (Figure 4, A and C) and occasional blebbing (Figure 4C). As reported by the size measures (Figure 3B), VPA induced nuclear elongation and flattening that were reflected in more ellipsoidal and less spherical shape. To quantify, by day 3, VPA-treated nuclei demonstrated lower sphericity (–3%, $p < 0.0001$, 72% AUC) and higher average mean curvature (+3%, $p < 0.0001$, 71% AUC), compared with the NHA group (Figure 4B), which indicated the presence of more convex and less concave points on the surface (Figure 4A). Average Gaussian curvature and curvedness of VPA-treated nuclei were slightly lower (–5%, $p < 0.05$, 58% AUC for Gaussian curvature; –5%, $p < 0.01$, 59% AUC for curvedness) than those of controls, which also corresponded to overall less spherical objects. Between days 3 and 5, there were similar intragroup decreases in sphericity, shape index, and solidity that corresponded to an increase in size of both treated and untreated nuclei at the same time point. More subtle alterations also included a decrease in average Gaussian curvature in both the NHA (–1%, $p < 0.05$) and the VPA (–5%, $p < 0.05$) groups, along with the decrease of fractal dimension of the untreated nuclei (–0.2%, $p < 0.01$; Figure 4B). Differences between shape descriptors extracted from two conditions on day 5 were similar to those from day 3. While the difference in solidity and shape index were not identified as "statistically significant" at the chosen *p*-value cutoffs, they contributed to the discriminative ability of the SVM classifier on both days 3 and 5 (Figure 2D), indicating their importance.

By day 7, NHA nuclei only demonstrated a 2% decrease in average mean curvature ($p < 0.05$) from the previous time point across all shape features. The VPA group exhibited an 11% decrease in curvedness ($p < 0.0001$) and a 7% decrease in average Gaussian curvature ($p < 0.01$; Figure 4B). As on days 3 and 5, treated nuclei

were still less spherical and had higher average mean curvature on day 7 compared with controls. However, decreases in curvedness (–15%, $p < 0.0001$, 74% AUC) and average Gaussian curvature (–10%, $p < 0.0001$, 71% AUC) were also more prominent at the last time point. Moreover, VPA-treated nuclei had 6% lower extent ($p < 0.01$, 64% AUC), and 0.2% lower fractal dimension ($p < 0.01$, 66% AUC), which indicated an overall higher global shape irregularity and less intensively folded and wrinkled nuclear surfaces, respectively.

Overall, we showed that VPA robustly induced more elongated and less spherical nuclear shapes with higher mean curvature from day 3. Toward day 7, these nuclei demonstrated more prominent deformations characterized, for example, by a kidney-like form and blebbing (Figure 4C). At the same time, the decrease in curvedness and fractal dimension reflected nuclear surfaces with lower local border complexity that has also been suggested to be indicative of chromatin decondensation, reduced tumorigenesis, and neuroprotection (Metze *et al.*, 2019). Combined with the size features, these 3D shape descriptors enable more accurate characterization of time-dependent morphological changes than their 2D counterparts or any single measure used individually.

Together, our findings described the dynamics of VPA-treated nuclear morphological profiles characterized by the increased sizes and progressively more irregular, complex shapes that can be attributed to altered histone modifications and chromatin decondensation. These observations represent a first step to studying time-dependent morphological effects of chromatin reorganization in the astrocyte-to-neuron reprogramming process and relating them to underlying molecular mechanisms. In future studies, this approach can be extended to label additional subnuclear components or organelles, such as nucleoli, chromosome territories, TADs, transcriptional condensates, and other compartments using, for example, cell painting assay(s) for high-content morphological profiling (Bray *et al.*, 2016). While tracking the overall cellular phenotype, this extension will allow us to include many other features in the models and assess their variability, association with cellular and nuclear shape morphology, disease state, and treatment conditions. All of this will set the stage to evaluate the effects of VPA and other small molecules measured with different concentrations and temporal sampling. Correlating these phenotypical cell and nuclear profiles with data from other assays, such as Hi-C (Lieberman-Aiden *et al.*, 2009), will likely provide useful insights into how altered functional properties of the genome are correlated with TAD structure, nuclear and cellular morphology, and whether it can be used for training machine learning models to more accurately predict treatment response in model systems and in humans (Kalinin *et al.*, 2018c).

MATERIALS AND METHODS

Request a protocol through *Bio-protocol*.

Sample preparation and image acquisition

Primary human astrocyte cells were purchased from ScienCell (human astrocytes hippocampal, catalog #1830).

Day 0:
Replace media with 50% growth media and 50% N2 media (DMEM/F12 + 1X pen/strep, 1X N2 supplements).

Day 1:
Control samples (NHA): for 30 ml of N2 media add 36 µl dimethyl sulfoxide (DMSO).

VPA-treated (1.5 mM VPA): for 30 ml of N2 media add 450 µl VPA

Day 3:
Collect day 3 control and VPA samples:

1. Fix samples in 4% paraformaldehyde (PFA) for 10 min.
2. Rinse three times for 5 min each in phosphate-buffered saline (PBS).
3. Store samples in PBS at 4°.

Control samples (NHA): for 30 ml of N2 media add 187.5 µl DMSO.

VPA-treated (1.5 mM VPA): for 30 ml of N2 media add 450 µl VPA.

Day 5:
Collect day 5 control and VPA samples:

1. Fix samples in 4% PFA for 10 min.
2. Rinse three times for 5 min each in PBS.
3. Store samples in PBS at 4°.

Control samples (NHA): for 30 ml of N2 media add 37.5 µl DMSO.

VPA-treated (1.5 mM VPA): for 30 ml of N2 media add 450 µl VPA.

Day 7:
Collect day 7 control and VPA samples:

1. Fix samples in 4% PFA for 10 min.
2. Rinse three times for 5 min each in PBS.
3. Store samples in PBS at 4°.

Cells in both collections were labeled with DAPI (4′,6-diamidino-2-phenylindole), a common stain for the nuclear DNA. 3D imaging employed a Zeiss LSM 710 laser scanning confocal microscope with a 63× PLAN/apochromat 1.4 NA DIC objective. Each original 3D volume was then resliced into a $1024 \times 1024 \times Z$ lattice ($Z = \{30,50\}$), where regional subvolumes facilitate the alignment with the native tile size of the microscope. For every subvolume, accompanying vendor metadata was extracted from the original data.

Image preprocessing and segmentation

To correct for imaging artifacts, including the effect of axial smearing on volumetric measures, we deconvolved the obtained images. Theoretical 3D point spread functions for each individual image volume were modeled using the Richards and Wolf algorithm from the PSFGenerator plugin for Fiji (Kirshner *et al.*, 2013). We then used estimated point spread functions and imaging metadata to apply Lucy-Richardson deconvolution (10 iterations) to the original 3D image volumes using the DeconvolutionLab2 software (Sage *et al.*, 2017). Deconvolution reduced axial smearing and improved segmentation and classification results (Supplemental Figure S1).

We performed the automatic 3D segmentation of nuclei from deconvolved images using the Nuclear Segmentation algorithm from the Farsight toolkit (Al-Kofahi *et al.*, 2010; Kalinin *et al.*, 2018a). The main advantage of this tool is that it was created specifically to segment DAPI-stained nuclei in 2D or 3D. Unlike other learning-based segmentation algorithms, it does not require a labeled training set. It demonstrated stable results in our previous project (Kalinin *et al.*, 2018a) and on these data. The algorithm implements multiple steps, which include a graph-cut algorithm to binarize the subvolumes, a multiscale Laplacian of Gaussian filter to convert the nuclei to blob masks, fast clustering to delineate the nuclei, and nuclear

contour refinement using graph cuts with α expansions (Al-Kofahi *et al.*, 2010).

After segmentation of the DAPI channel subvolumes, data were converted to 16-bit 3D TIFF files; each segmented nucleus was represented as a binary mask, and given a unique index value. Postsegmentation processing of nuclear masks included 3D hole filling and a filtering step that removed the objects if they span the edge of a tile or are connected to other objects. This quality control protocol filtered out most of the artifacts and the remaining were removed by visual inspection.

3D morphometry

3D binary nuclear masks were then used for voxel-based feature extraction using the scikit-image Python library (van der Walt *et al.*, 2014), obtaining feature set *V*. For each binary mask, we measured nuclear volume, bounding box and convex hull volumes, extent, solidity, lengths of principal axes, inertia tensor principal components, and diameter of the sphere with the same volume as the nucleus. To compare the performance of 2D versus 3D features, we also extracted 2D features from maximum intensity projections of binary masks.

First, we model the boundaries of nuclear 3D masks extracted from the microscopic images as genus zero two-dimensional manifolds that are embedded as triangulated surfaces in $\mathbf{R}^3$ (Kalinin *et al.*, 2018b). 3D surface modeling uses an iterative Laplace-Beltrami eigenprojection and a topology-preserving boundary deformation algorithm (Shi *et al.*, 2010). This algorithm performs robust reconstruction of the objects' surfaces from their segmented masks using an iterative mask filtering process. We used Mask2Mesh implementation of this algorithm from the MOCA framework (Shi *et al.*, 2010) and then applied mesh simplification and subdivision to 40,000 triangles, following the shape analysis protocol in Kalinin *et al.* (2018b). The next step included the extraction of geometric characteristics of the 3D nuclear surfaces (e.g., mesh volume, surface area, curvedness, shape index, and fractal dimension), implemented in Laboratory of Neuro Imaging Pipeline v7.0.3 (Dinov *et al.*, 2009; Kalinin *et al.*, 2018b). To provide a comprehensive morphological characterization, we expanded the list of six metrics previously reported in Kalinin *et al.* (2018b). The additional surface features were extracted using the trimesh library (Dawson-Haggerty and GitHub open-source software contributors, 2019) and included average mean curvature, convex hull and bounding primitive (box, oriented box, cylinder, sphere) volumes, convex hull surface area, inertia tensor eigenvalues, and principal axes lengths. Surface-based extent and solidity were computed from trimesh-derived measures as the ratio of the object volume to the bounding box volume and the ratio of the object volume to the convex hull volume, correspondingly. Sphericity of the nucleus was computed as the ratio of the surface area of a sphere with the same volume as the given nucleus to the surface area of the nucleus: $\Psi = \frac{\pi^{\frac{1}{3}}(6V)^{\frac{2}{3}}}{SA}$, where V is the volume of the nucleus and SA is the surface area of the nucleus (Wadell, 1935). All surface descriptors were combined into the feature set *S*.

Both volumetric and surface features we merged by inner join on the per-nucleus basis, filtering out those individual cells, for which feature extraction failed or voxel volume measure exceeded the empirically estimated threshold of 150,000 voxels. Nuclei were also considered outliers and removed if any feature value computed over all cells was out of the $[P_5 - 1.5(P_{95} - P_5);\ P_{95} + 1.5(P_{95} - P_5)]$ range, where P_5 and P_{95} are 5th and 95th percentiles, correspondingly. All extracted features were aggregated into per-nucleus feature vectors, from which we constructed a feature table per each day of treatment with the labels corresponding to phenotypic conditions (NHA and VPA).

Feature and model selection, and analysis

To handle multicollinear features, we performed hierarchical clustering on the Spearman rank-order correlations between all features and then used averaged SVM classification performance to select a threshold for defining feature clusters, while controlling for overfitting with fivefold statistical cross-validation repeated from five different random seeds. From each cluster, we selected one feature according to the highest value for the χ^2 statistic, while ignoring inertia tensor eigenvalues, as they were highly correlated with other features that are easier to directly interpret, such as volume or minimal principal axis length. This process yielded the final set S_7 consisting of the following seven descriptors: surface-based median axis length, convex hull and bounding sphere volumes, sphericity, average mean curvature, shape index, and voxel-based solidity. t-SNE embedding was generated using the scikit-learn library (Pedregosa *et al.*, 2011) with PCA initialization, perplexity of 13, and cosine distance as a metric. Clusters for each condition at every time point were identified using kernel density estimation in the seaborn library (Waskom *et al.*, 2020) with 0.75 threshold. It should be noted that cluster sizes and intercluster distances should be interpreted with care when using t-SNE (Wattenberg *et al.*, 2016).

The following sets of features were used to compare volumetric and surface-based shape representations: V_{2D}, V, S, V_{sub}, S_{sub}, V+S, S_7, where V_{sub} and S_{sub} were subsets of equivalent voxel and surface feature sets correspondingly (nuclear volume, convex hull and bounding box volumes, extent, solidity, inertia eigenvalues, and major axis length). We assessed the classification performance of those classifiers with the scikit-learn library (Pedregosa *et al.*, 2011) that provided feature weights as an output. These included Gaussian naïve Bayes, *k*-nearest neighbors, logistic regression, linear SVM, random forest, extremely randomized trees, AdaBoost and gradient boosting machine. They were trained using default hyperparameter values and evaluated at each time point using the AUC. AUCs, confusion matrices, and feature ranking were averaged from 10 repetitions of the internal statistical fivefold stratified cross-validation with different random seeds. We averaged the performance of each model over time points and over all feature sets. To compare feature sets, we averaged the AUCs over all models and days. Random subsampling of the prevalent class by the total number of per-fold training samples from an underrepresented class at each iteration of the cross-validation procedure was used to combat class imbalance. To rank features by their relative importance, we employed the permutation importance strategy that reflects the decrease in a model performance when a single feature value is randomly shuffled (Breiman, 2001). This breaks the relationship between the feature and the outcome, while being model agnostic and can be calculated many times with different permutations of the feature. We computed permutation importance on a held-out set on each cross-validation cycle, highlighting which features contribute the most to the generalization power of the trained model. Permutation feature importance was computed using the "*coef*" property of the trained SVM model at each time point.

Univariate statistical analysis of individual features was performed using the SciPy package (Virtanen *et al.*, 2020) with multiple testing correction using statsmodels (Seabold and Perktold, 2010). We reported each relative difference as the percentage change from the control group, along with a *p* value obtained using a two-sided Mann-Whitney *U* test with Holm–Šidák multiple

testing correction ($\alpha = 0.05$), and the common language effect size statistic that in the case of the Mann-Whitney *U* test is equivalent to the AUC (Mason and Graham, 2002).

For all analysis tasks we used Python 3.8.3 from the Anaconda distribution (Continuum Analytics and others, 2020), with the *numpy* (van der Walt *et al.*, 2011), pandas (McKinney, 2010), and iPython (Perez and Granger, 2007) packages. Image processing was done using scikit-image (van der Walt *et al.*, 2014). Visualizations and charts were built with the matplotlib (Hunter, 2007), seaborn (Waskom *et al.*, 2020), trimesh (Dawson-Haggerty and GitHub open-source software contributors, 2019), and SOCRAT (Kalinin *et al.*, 2017) libraries.

The documentation supporting the conclusions of this article together with the derived data, pipeline workflows, and underlying source code is made publicly available online on the project webpage: SOCR 3D Cell Morphometry Project, https://socr.umich.edu/projects/3d-cell-morphometry.

ACKNOWLEDGMENTS

The authors thank Ari Allyn-Feuer, Samuel Handelman, and Gilbert Omenn for thoughtful discussions and helpful suggestions. We thank colleagues at the Laboratory of Neuro Imaging (LONI), Keck School of Medicine, University of Southern California, for providing technical support for the LONI Pipeline environment. This work is supported by Chinese Key-Area Research and Development Program of Guangdong Province (2020B0101350001). This work was also partially supported by the National Science Foundation Grants no. 1916425, no. 1734853, no. 1636840, no. 1416953, no. 0716055, and no. 1023115; the National Institutes of Health Grants no. P20 NR-015331, no. P30 DK-089503, no. UL1TR-002240, no. R01CA-233487, and no. R01MH-121079. Xin Rong of the University of Michigan donated NVIDIA TITAN X GPU used for this research, and the NVIDIA Corporation donated the TITAN Xp GPU used to execute the computationally intensive protocol.

REFERENCES

Al-Kofahi Y, Lassoued W, Lee W, Roysam B (2010). Improved automatic detection and segmentation of cell nuclei in histopathology images. IEEE Trans Biomed Eng 57, 841–852.

Amamoto R, Arlotta P (2014). Development-inspired reprogramming of the mammalian central nervous system. Science 343, 1239882.

Bray M-A, Singh S, Han H, Davis CT, Borgeson B, Hartland C, Kost-Alimova M, Gustafsdottir SM, Gibson CC, Carpenter AE (2016). Cell painting, a high-content image-based assay for morphological profiling using multiplexed fluorescent dyes. Nat Protoc 11, 1757–1774.

Breiman L (2001). Random forests. Mach Learn 45, 5–32.

Chen H, Chen J, Muir LA, Ronquist S, Meixner W, Ljungman M, Ried T, Smale S, Rajapakse I (2015). Functional organization of the human 4D nucleome. Proc Natl Acad Sci USA 112, 8002–8007.

Cheng L, Gao L, Guan W, Mao J, Hu W, Qiu B, Zhao J, Yu Y, Pei G (2015). Direct conversion of astrocytes into neuronal cells by drug cocktail. Cell Res 25, 1269.

Choi H-J, Choi H-K (2007). Grading of renal cell carcinoma by 3D morphological analysis of cell nuclei. Comput Biol Med 37, 1334–1341.

Continuum Analytics and others (2020). Anaconda software distribution. Computer software version 2-2.4.0, https://docs.anaconda.com.

Cortes C, Vapnik V (1995). Support-vector networks. Mach Learn 20, 273–297.

Cremer T, Cremer M, Hübner B, Strickfaden H, Smeets D, Popken J, Sterr M, Markaki Y, Rippe K, Cremer C (2015). The 4D nucleome: evidence for a dynamic nuclear landscape based on co-aligned active and inactive nuclear compartments. FEBS Lett 589, 2931–2943.

Dawson-Haggerty and GitHub open-source software contributors (2019). trimesh (software). https://github.com/mikedh/trimesh

Depeursinge A, Foncubierta-Rodriguez A, Van De Ville D, Müller H (2014). Three-dimensional solid texture analysis in biomedical imaging: Review and opportunities. Med Image Anal 18, 176–196.

Dinov I, Van Horn J, Lozev K, Magsipoc R, Petrosyan P, Liu Z, MacKenzie-Graha A, Eggert P, Parker DS, Toga AW (2009). Efficient, distributed and interactive neuroimaging data analysis using the LONI pipeline. Frontiers Neuroinf 3, 22.

Dufour AC, Liu T-Y, Ducroz C, Tournemenne R, Cummings B, Thibeaux R, Guillen N, Hero AO, Olivo-Marin J-C (2015). Signal processing challenges in quantitative 3-d cell morphology: more than meets the eye. IEEE Signal Process Mag 32, 30–40.

Eckschlager T, Plch J, Stiborova M, Hrabeta J (2017). Histone deacetylase inhibitors as anticancer drugs. Int J Mol Sci 18, 1414.

Felisbino MB, Costa TA, Gatti MSV, Mello MLS (2016). Differential response of human hepatocyte chromatin to HDAC inhibitors as a function of microenvironmental glucose level. J Cell Physiol 231, 2257–2265.

Felisbino MB, Gatti MSV, Mello MLS (2014). Changes in chromatin structure in NIH 3T3 cells induced by valproic acid and trichostatin A. J Cell Biochem 115, 1937–1947.

Felisbino MB, Tamashiro W, Mello MLS (2011). Chromatin remodeling, cell proliferation and cell death in valproic acid-treated HeLa cells. PLoS One 6, e29144.

Ganai SA, Malli Kalladi S, Mahadevan V (2015). HDAC inhibition through valproic acid modulates the methylation profiles in human embryonic kidney cells. J Biomol Struct Dyn 33, 1185–1197.

Gao L, Guan W, Wang M, Wang H, Yu J, Liu Q, Qiu B, Yu Y, Ping Y, Bian X, *et al.* (2017). Direct generation of human neuronal cells from adult astrocytes by small molecules. Stem Cell Rep 8, 538–547.

Göttlicher M, Minucci S, Zhu P, Krämer OH, Schimpf A, Giavara S, Sleeman JP, Coco FL, Nervi C, Pelicci PG, *et al.* (2001). Valproic acid defines a novel class of HDAC inhibitors inducing differentiation of transformed cells. EMBO J 20, 6969–6978.

Higgins GA, Allyn-Feuer A, Georgoff P, Nikolian V, Alam HB, Athey BD (2017a). Mining the topography and dynamics of the 4D Nucleome to identify novel CNS drug pathways. Methods 123, 102–118.

Higgins GA, Allyn-Feuer A, Handelman S, Sadee W, Athey BD (2015). The epigenome, 4D nucleome and next-generation neuropsychiatric pharmacogenomics. Pharmacogenomics 16, 1649–1669.

Higgins GA, Georgoff P, Nikolian V, Allyn-Feuer A, Pauls B, Higgins R, Athey BD, Alam HE (2017b). Network reconstruction reveals that valproic acid activates neurogenic transcriptional programs in adult brain following traumatic injury. Pharm Res 34, 1658–1672.

Huangfu D, Maehr R, Guo W, Eijkelenboom A, Snitow M, Chen AE, Melton DA (2008). Induction of pluripotent stem cells by defined factors is greatly improved by small-molecule compounds. Nat Biotechnol 26, 795–797.

Hunter JD (2007). Matplotlib: a 2D graphics environment. Comput Sci Eng 9, 90–95.

Kalinin AA, Allyn-Feuer A, Ade A, Fon GV, Meixner W, Dilworth D, De Wet JR, Higgins GA, Zheng G, Creekmore A, *et al.* (2018a). 3D cell nuclear morphology: microscopy imaging dataset and voxel-based morphometry classification results. In: Proceedings of the IEEE Conference on Computer Vision and Pattern Recognition Workshops, 2272–2280.

Kalinin AA, Allyn-Feuer A, Ade A, Fon GV, Meixner W, Dilworth D, Husain SS, Jeffrey R, Higgins GA, Zheng G, *et al.* (2018b). 3D shape modeling for cell nuclear morphological analysis and classification. Sci Rep 8, 13658.

Kalinin AA, Higgins GA, Reamaroon N, Soroushmehr S, Allyn-Feuer A, Dinov ID, Najarian K, Athey BD (2018c). Deep learning in pharmacogenomics: from gene regulation to patient stratification. Pharmacogenomics 19, 629–650.

Kalinin AA, Palanimalai S, Dinov ID (2017). SOCRAT platform design: a web architecture for interactive visual analytics applications. In: Proceedings of the 2nd Workshop on Human-In-the-Loop Data Analytics, New York: ACM, 8:1–8:6.

Kirshner H, Aguet F, Sage D, Unser M (2013). 3-D PSF fitting for fluorescence microscopy: implementation and localization application. J Microsc 249, 13–25.

Koenderink JJ, Van Doorn AJ (1992). Surface shape and curvature scales. Image Vis Comput 10, 557–564.

Kortenhorst MSQ, Isharwal S, van Diest PJ, Chowdhury WH, Marlow C, Carducci MA, Rodriguez R, Veltri RW (2009). Valproic acid causes dose- and time-dependent changes in nuclear structure in prostate cancer cells *in vitro* and *in vivo*. Mol Cancer Ther 8, 802–808.

Lieberman-Aiden E, Van Berkum NL, Williams L, Imakaev M, Ragoczy T, Telling A, Amit I, Lajoie BR, Sabo PJ, Dorschner MO, *et al.* (2009). Comprehensive mapping of long-range interactions reveals folding principles of the human genome. Science 326, 289–293.

Marchion DC, Bicaku E, Daud AI, Sullivan DM, Munster PN (2005). Valproic acid alters chromatin structure by regulation of chromatin modulation proteins. Cancer Res 65, 3815–3822.
Mason SJ, Graham NE (2002). Areas beneath the relative operating characteristics (ROC) and relative operating levels (ROL) curves: statistical significance and interpretation. Q J R Meteorol Soc 128, 2145–2166.
McKinney W (2010). Data structures for statistical computing in Python. In: Proceedings of the 9th Python in Science Conference, 56–61.
Medyukhina A, Blickensdorf M, Cseresnyés Z, Ruef N, Stein JV, Figge MT (2020). Dynamic spherical harmonics approach for shape classification of migrating cells. Sci Rep 10, 6072.
Metze K, Adam R, Florindo JB (2019). The fractal dimension of chromatin—a potential molecular marker for carcinogenesis, tumor progression and prognosis. Expert Rev Mol Diagn 19, 299–312.
Meyer MG, Fauver M, Rahn JR, Neumann T, Patten FW, Seibel EJ, Nelson AC (2009). Automated cell analysis in 2D and 3D: a comparative study. Pattern Recogn 42, 141–146.
Olson RS, Cava WL, Mustahsan Z, Varik A, Moore JH (2018). Data-driven advice for applying machine learning to bioinformatics problems. In: Biocomputing 2018, Kohala Coast, Hawaii: World Scientific, 192–203.
Pedregosa F, Varoquaux G, Gramfort A, Michel V, Thirion B, Grisel O, Blondel M, Prettenhofer P, Weiss R, Dubourg V, *et al*. (2011). Scikit-learn: machine learning in Python. J Mach Learn Res 12, 2825–2830.
Perez F, Granger BE (2007). IPython: a system for interactive scientific computing. Comput Sci Eng 9, 21–29.
Pickell Z, Williams AM, Alam HB, Hsu CH (2020). Histone deacetylase inhibitors: a novel strategy for neuroprotection and cardioprotection following ischemia/reperfusion injury. J Am Heart Assoc 9, e016349.
Qin H, Zhao A, Fu X (2017). Small molecules for reprogramming and transdifferentiation. Cell Mol Life Sci 74, 3553–3575.
Sage D, Donati L, Soulez F, Fortun D, Schmit G, Seitz A, Guiet R, Vonesch C, Unser M (2017). DeconvolutionLab2: an open-source software for deconvolution microscopy. Methods 115, 28–41.
Sasai K, Akagi T, Aoyanagi E, Tabu K, Kaneko S, Tanaka S (2007). O6-methylguanine-DNA methyltransferase is downregulated in transformed astrocyte cells: implications for anti-glioma therapies. Mol Cancer 6, 36.
Seabold S, Perktold J (2010). statsmodels: econometric and statistical modeling with Python. In: 9th Python in Science Conference.
Shi Y, Lai R, Morra JH, Dinov I, Thompson PM, Toga AW (2010). Robust surface reconstruction via Laplace-Beltrami eigen-projection and boundary deformation. IEEE Trans Med Imag 29, 2009–2022.
Stephens AD, Banigan EJ, Adam SA, Goldman RD, Marko JF (2017). Chromatin and lamin A determine two different mechanical response regimes of the cell nucleus. Mol Biol Cell 28, 1984–1996.
Stephens AD, Banigan EJ, Marko JF (2019). Chromatin's physical properties shape the nucleus and its functions. Curr Opin Cell Biol 58, 76–84.
Stephens AD, Liu PZ, Banigan EJ, Almassalha LM, Backman V, Adam SA, Goldman RD, Marko JF (2018). Chromatin histone modifications and rigidity affect nuclear morphology independent of lamins. Mol Biol Cell 29, 220–233.
Tsagkrasoulis D, Hysi P, Spector T, Montana G (2017). Heritability maps of human face morphology through large-scale automated three-dimensional phenotyping. Sci Rep 7, 45885.
Uhler C, Shivashankar GV (2018). Nuclear mechanopathology and cancer diagnosis. Trends Cancer 4, 320–331.
van der Maaten L, Hinton G (2008). Visualizing data using t-SNE. J Mach Learn Res 9, 2579–2605.
van der Walt S, Colbert SC, Varoquaux G (2011). The NumPy array: a structure for efficient numerical computation. Comput Sci Eng 13, 22–30.
van der Walt S, Schönberger JL, Nunez-Iglesias J, Boulogne F, Warner JD, Yager N, Gouillart E, Yu T (2014). scikit-image: image processing in Python. PeerJ 2, e453.
Virtanen P, Gommers R, Oliphant TE, Haberland M, Reddy T, Cournapeau D, Burovski E, Peterson P, Weckesser W, Bright J, *et al*. (2020). SciPy 1.0: fundamental algorithms for scientific computing in Python. Nat Methods 17, 261–272.
Wadell H (1935). Volume, shape, roundness of quartz particles. J Geol 43, 250–280.
Waskom M, Botvinnik O, Ostblom J, Gelbart M, Lukauskas S, Hobson P, Gemperline DC, Augspurger T, Halchenko Y, Cole JB, *et al*. (2020). mwaskom/seaborn: v0.10.1 (April 2020), Zenodo.
Wattenberg M, Viégas F, Johnson I (2016). How to use t-SNE effectively. Distill 1, e2.
Xu D, Cui J, Bansal R, Hao X, Liu J, Chen W, Peterson BS (2009). The ellipsoidal area ratio: an alternative anisotropy index for diffusion tensor imaging. Magn Reson Imaging 27, 311–323.
Yang X-J, Seto E (2007). HATs and HDACs: from structure, function and regulation to novel strategies for therapy and prevention. Oncogene 26, 5310–5318.
Yin JC, Zhang L, Ma NX, Wang Y, Lee G, Hou XY, Lei ZF, Zhang FY, Dong FP, Wu GY, *et al*. (2019). Chemical conversion of human fetal astrocytes into neurons through modulation of multiple signaling pathways. Stem Cell Rep 12, 488–501.
Zhang L, Yin JC, Yeh H, Ma NX, Lee G, Chen XA, Wang Y, Lin L, Chen L, Jin P, *et al*. (2015). Small molecules efficiently reprogram human astroglial cells into functional neurons. Cell Stem Cell 17, 735–747.